



Optics Letters

112° field of view high-resolution swept-source OCT angiography for rat retinas

GUANGRU B. LIANG,^{1,2} SHuibin Ni,^{1,2} TRISTAN T. HORMEL,¹ JOHN C. MORRISON,¹ DIANA C. LOZANO,¹ YIFAN JIAN,^{1,2} J. PETER CAMPBELL,¹ AND YALI JIA^{1,2,*}

¹ Casey Eye Institute, Oregon Health & Science University, Portland, Oregon 97239, USA

² Department of Biomedical Engineering, Oregon Health & Science University, Portland, Oregon 97239, USA

*jiaya@ohsu.edu

Received 31 July 2024; revised 14 October 2024; accepted 14 October 2024; posted 16 October 2024; published 6 November 2024

This study introduces an ultra-wide field (UWF) and high-resolution swept-source optical coherence tomographic angiography (OCTA) system for rat retinal imaging. Using an asymmetrical optics design, the system achieves unprecedented details of retinal structures and vascular plexuses over a large field of view (112°) in a single-shot acquisition. Views of single-nerve fiber bundles and single capillary vessels are consistently visible over a 112° field of view. The system has a long imaging range and high penetration and allows a full view of vitreous hyaloid vessels, retina, choroid, sclera, and posterior ciliary arteries, down to sub-sclera connective tissues. In a longitudinal study of oxygen-induced retinopathy (OIR) in rats, the system successfully revealed the progression and regression of OIR-related vascular pathologies, such as ischemia, neovascularization, and tortuosity. To our knowledge, this novel UWF-OCT/OCTA prototype designed for rat retinal imaging will be a vital tool for monitoring disease progression and evaluating therapeutic interventions in preclinical models.

© 2024 Optica Publishing Group under the terms of the [Optica Open Access Publishing Agreement](#)

<https://doi.org/10.1364/OL.538165>

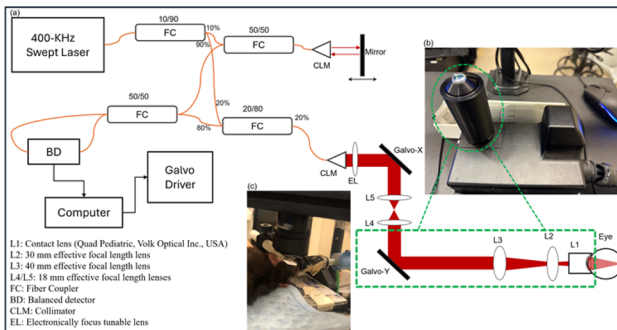
Rats are widely used to study retinal circulation and ocular disease pathophysiology. Their retinal structures share many similarities with human anatomy, including neural tissue layers and vascular plexuses. Furthermore, their retinal vasculature develops postnatally [1], ideal for studying retinopathy of prematurity (ROP). In addition, various rat strains exist that mimic various forms of inherited retinal degeneration found in humans.

Several imaging technologies, such as scanning laser ophthalmoscopy (SLO), fluorescence angiography (FA), and adaptive optics (AO), have made significant contributions to understanding retinal vascular diseases in rat models by enabling *in-vivo* visualization of the retina and longitudinal monitoring of its development [2,3]. However, despite being able to observe pathological abnormalities, these technologies do not provide three-dimensional vasculatures. For instance, they cannot provide flexible cross-sectional imaging options comparable to a histological analysis [4]. In addition, SLO and FA require external contrast agents, and AO has a very small field of view (FOV).

By comparison, optical coherence tomography (OCT) offers three-dimensional, depth-resolved imaging. Its variant specialized for vascular imaging, OCT angiography (OCTA), provides the additional advantage of capturing *in-vivo* blood flow in retinal and choroidal tissues by computing motion contrast through sequential scans from identical locations. This enables the label-free detection of vascular structure down to the capillary, making it particularly advantageous for a detailed, longitudinal analysis in small animals.

Nonetheless, current OCTA technology in rat models has a limited FOV, inferior to flat-mount histological methods. This limitation severely hinders investigations of structural and vascular changes in peripheral regions. These areas show the earliest progression in diseases such as diabetic retinopathy (DR), and ROP [5]. While wide-field OCTA systems for human imaging have been shown to excel in identifying pathologies such as ischemia, vessel tortuosity, and neovascularization [6], such advances have not been developed for rat imaging.

Unlike histology, where focal optics systems allow lateral movements to expand the FOV, *in-vivo* retinal imaging must account for the optics of the subject's eye, requiring continuous realignment. Typically, a wider FOV is achieved by an afocal relay system to magnify the scanning angle of the galvo scanner, enabling a broader coverage of the retina [7]. Two key design considerations come into play for constructing an effective wide-field lens. First, an appropriate relay angle amplification factor is crucial to balance the FOV extension, resolution, and minimization of aberration. Second, the scanning pivot point should be positioned near the pupil plane to mitigate the risk of iris vignetting. Most retinal OCT systems employ a 4f system: a symmetrical optics layout with two focusing lens groups separated by the sum of their focal lengths, with the system's rear focal point at the scanner. The scanning angle is subsequently amplified by a factor of the ratio of the groups' effective focal lengths, with the scanning pivot point near the system's front focal point. The 4f relay system has achieved wide-field imaging in several human retinal OCT systems [7–10]. However, in rat imaging, the smaller eye size limits the incident angle for light entering the cornea, restricting the field aperture to the cornea's size, which limits a large FOV. In our previous study, we achieved a 50° FOV by montaging different scans [11], a common approach in many commercial human OCT systems



[12,13]. However, *in-vivo* retinal montaging in the anesthetized rat is more challenging, since unlike the human, a rat cannot adjust its eye fixation to different targets on demand.

In this Letter, we introduce a novel single-shot ultra-wide field (UWF) OCTA system for rat retinal imaging. Instead of a conventional $4f$ relay, this system uses an asymmetrical optical configuration. This design optimizes the imaging probe relay's efficiency, significantly expanding the FOV to 112° , while maintaining high resolution and minimizing aberrations.

The design of this system (Fig. 1) was modified from a handheld OCTA system previously developed in our lab [10]. It uses a 400-kHz vertical cavity surface emitting laser (SVM10F-0210, Thorlabs Inc.). The swept-source laser has a 100-nm bandwidth with a center wavelength of 1060 nm, corresponding to a maximum axial resolution of $5\text{ }\mu\text{m}$ in air. In the UWF scan lens design, a high-focus power contact lens [L1 in Figs. 1(a) and 2(a), Quad Pediatric, custom near-infrared coating, Volk Optical Inc.] is employed to maximize the incident beam directed onto the cornea [14]. Concurrently, the lens group L2 ($2 \times$ AC300-060-B, Thorlabs Inc.) aims to align the pivot point with the pupil plane eliminating iris vignetting. Meanwhile, the L3 lens group ($2 \times$ AC300-080-B, Thorlabs Inc.) functions as an objective lens to gather light from the galvo scanner. Together, these elements compose a $4.7\times$ telescope with an asymmetrical optical configuration that effectively overcomes the constraints in rat retinal wide-field imaging that a common $4f$ setup has not achieved. A second relay telescope (L4 and L5 in Fig. 1(a), $4 \times$ AC254-35-B, Thorlabs Inc.) is placed between the two scanning mirrors to reduce beam wandering in the pupil plane.

The sample arm of the UWF-OCTA system was optimized in OpticStudio (Ansys Inc.), using a rat eye optical model [15] to analyze aberrations and performance across various scanning angles. The beam size is 0.47 mm at the cornea, resulting in a theoretical lateral resolution of $8.9\text{ }\mu\text{m}$ (Airy disk radius) on the retina for a rat with an axial length of 6.1 mm , and the angular FOV is defined by the scanning angle at the pivot point. The $4.7\times$ magnification factor is calculated using the beam

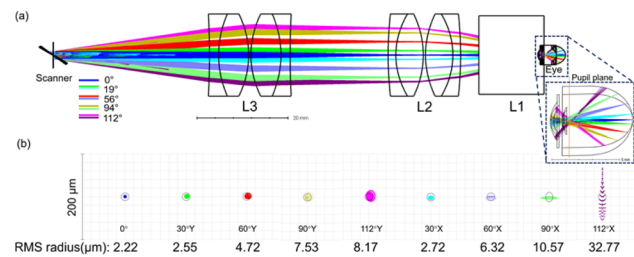


Fig. 2. Optical simulation of our designed imaging probe in OpticStudio. (a) Three-dimensional layout of the sample arm design with colored beams corresponding to different scanning angles in the orthogonal x and y directions. (b) Multi-configuration spot diagrams for the optical design; the radius of Airy disk (black circle) is $8.9\text{ }\mu\text{m}$.

diameters at the surfaces after the scanner and the pivot point. Spot diagrams at different angular FOVs are shown in Fig. 2(b) demonstrating effective aberration control up to 90° . Beyond this, aberrations such as astigmatism, coma, and field curvature become noticeable, particularly along the x axis due to the second relay telescope. While these aberrations are inherent to the expanded FOV, the capability to reach such wide imaging angles is a unique feature not attainable by conventional systems.

We use a unidirectional raster scan for this project, with 2048 pixels per A-line (6 mm maximum imaging range in air), 1200 A-scans per B-scan, three repeated B-scans for OCTA, and a total of 1200 B-scan locations, resulting in an average lateral sampling density of $5\text{ }\mu\text{m}/\text{pixel}$. With a 3 ms interval between repeated B-scans, each volume takes 10.8 s to complete. Acquired spectrum data are processed and displayed in real-time OCT images with previously developed acquisition software [16]. OCTA volumes are produced post-acquisition using the split-spectrum amplitude decorrelation angiography algorithm [17], and segmentation is conducted automatically by a neural network [18] to generate en face projections of specific layers.

We imaged two healthy adult Brown Norway rats, as well as six oxygen-induced retinopathy (OIR) rats and an age-matched control, using the UWF OCTA system. The OIR rats were induced using a modified 50%/10% oxygen exposure paradigm [19] to model the ROP.

In brief, newborn pups were transferred with their dams to an air chamber that alternates hyperoxia (50% O_2) and hypoxia (10% O_2) every 24 h for 21 days, with continuous exposure interrupted only for animal care. After that, the rats were released into a normal air environment (21% O_2). The age-matched healthy controls were raised in normal air condition (21% O_2). Before imaging, a 1% tropicamide ophthalmic solution was applied to dilate the pupil, together with a lubricant eye gel to improve the optical quality. During imaging, subjects were anesthetized with inhaled 2.5% isoflurane and were kept in a warm blanket circulated with 37°C water to maintain body temperature and comfort. All procedures involving animal experiments were conducted in accordance with the Association for Research in Vision and Ophthalmology statement for the use of animals in ophthalmic and vision research and were approved by the Institutional Animal Care and Use Committee of Oregon Health & Science University.

Retinal images of mature healthy Brown Norway rats (~20-weeks-old, ~270 g, N = 2) with a 112° FOV are demonstrated in representative scans in Figs. 3 and 4. Individual nerve fiber bundles [Fig. 3(c)] and single capillaries [Fig. 3(f)] could be

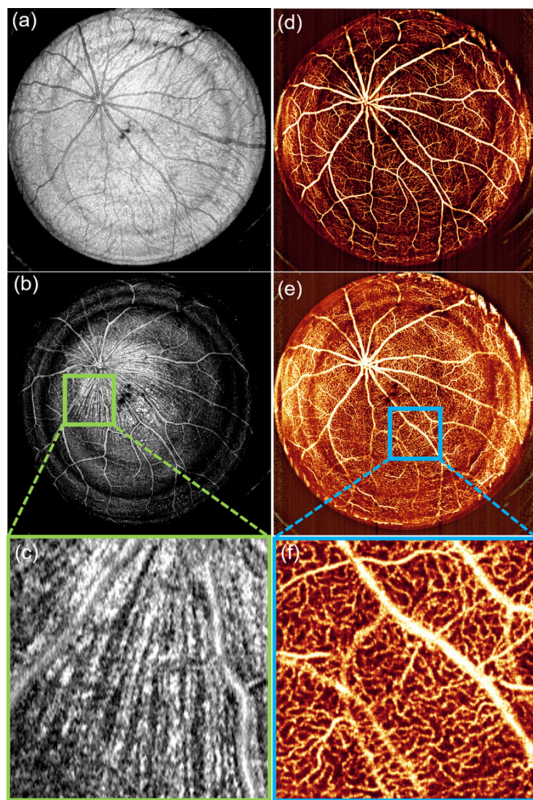


Fig. 3. 112° high resolution *en face* retinal images of a mature healthy Brown Norway rat. (a) OCT projection of the whole retina, exemplifying the large FOV that can be achieved. (b) OCT projection of the nerve fiber layer. (c) Cropped images from the highlighted region in (b), with clear differentiation of individual nerve fiber bundles, demonstrating the high lateral resolution achieved by the system. (d) OCTA projection of the superficial vascular layer. (e) OCTA projection of the deep vascular layer. (f) Cropped images from the highlighted region in (e), showing detailed capillaries with its lobular nature.

captured by the UWF system with 8.9-μm lateral resolution. Additionally, the system's deep tissue penetration capabilities were highlighted in Fig. 4, showing OCTA projection of the choroidal vasculature [Fig. 4(a)] and OCT projection of sub-scleral tissue [Fig. 4(b)]. The cross-sectional image [Fig. 4(c)] further shows clear differentiation of multiple retinal layers and sub-retinal structures, including choroid, choroidal vessels, choroid/sclera boundary, posterior ciliary arteries, extraocular muscles, and connective tissue. Visualizing the choroidal vasculature and sub-retinal tissue could also potentially reveal the roles of these structures in retinal pathology.

Thanks to the non-invasive nature of OCT/OCTA, the UWF-OCTA system was additionally utilized to longitudinally image OIR rats and a healthy age-matched control rat. Images were acquired at three different time points (postnatal day 27, day 31, and day 38). The representative images acquired from an OIR rat revealed non-perfusion areas, reduced vessel density, and tortuous vessels at day 27 and day 31, compared to the age-matched control (Fig. 5). The non-perfusion areas and tortuous vessels gradually decreased by day 38, indicating a regression of retinopathy. These vascular changes are similar to those seen in human ROP patients undergoing spontaneous regression [20].

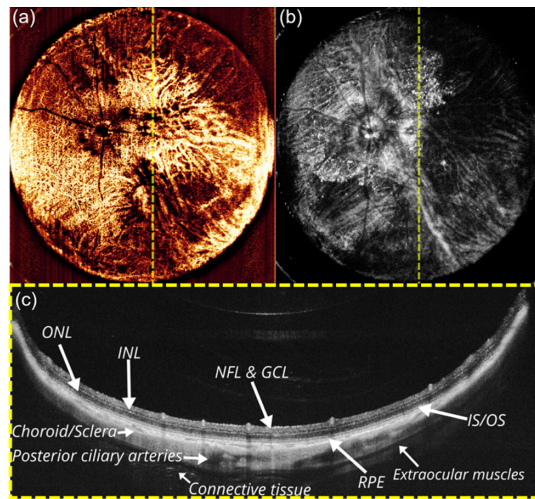


Fig. 4. Deep tissue penetration for visualizing sub-retinal structures from a mature healthy rat. (a) OCTA projections of choroid. (b) OCT projections of sub-scleral tissue. These images underscore the system's enhanced penetration depth and ability to detail structures beyond the retina. (c) Cross-sectional image at the plane marked by yellow lines in (a) and (b), showing clear differentiation of multiple retinal layers. NFL, nerve fiber layer; GCL, ganglion cell layer; INL, inner plexiform layer; ONL, outer nuclear layer; IS/OS, inner/outer segment; RPE, retinal pigment epithelium.

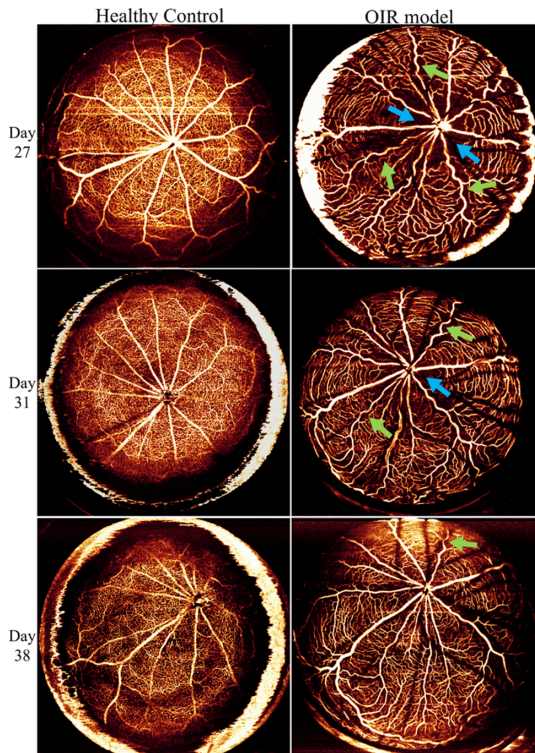


Fig. 5. 112° high-resolution *en face* inner retinal OCTA images of a Brown Norway rat age-matched control and an OIR rat taken by the UWF-OCTA system at three different time points. Tortuous vessels (green arrows) and non-perfusion areas (blue arrows) can be observed in the OIR rat, with tortuosity decreasing and vessel density increasing over time, returning to healthy levels.

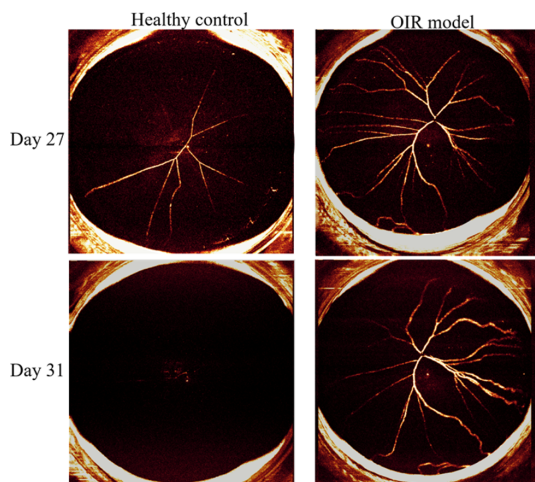


Fig. 6. OCTA projections of vitreous hyaloid vessels from an age-matched control and OIR rats at two different time points. The images exhibit abnormal lingering hyaloid vasculature in an OIR rat on day 31 post-birth.

With the 6-mm imaging range and enhanced penetration of the 1060 nm swept-source system, we were also able to visualize the hyaloid vessels (the fetal blood vessels supplying the developing lens) in the vitreous (Fig. 6), choroidal vessels, and tissues beyond the sclera [Fig. 4(c)]; e.g., by post-natal day 31, the hyaloid vessel had regressed in healthy rats but remained visible in OIR rats, consistent with prior findings [21].

Despite these compelling results, the current system design has limitations. The contact-based imaging probe stabilizes the subject's eye during imaging, but it limits the ability to adjust fine alignment. Operators must retract the probe to adjust the imaging position, which can introduce air bubbles between the probe and the lubricated eye, thereby disrupting the signal (as shown in Fig. 3, where air bubbles caused dark spots in the center). Additionally, it was difficult to image young rats because they kept their eyes closed for prolonged periods of time after birth. A specialized eyelid holder will be needed to stabilize and keep the eye open. This will allow for undisturbed and effective alignment, while ensuring uniformity and quality of retinal images across all subjects. Future work also needs a quantitative validation of the system's FOV and lateral resolution. While simple eye models with off-the-shelf lenses can evaluate idealized paraxial performance, they are unrealistic for our study (*Supplement 1*). Therefore, the actual FOV and lateral resolution will be evaluated using the corresponding histological sections.

In conclusion, an ultra-wide field and high-resolution swept-source OCTA system has been developed for rat retinal imaging. We achieve 112° high-resolution OCT/OCTA imaging of the rat retina by implementing an asymmetrical optics configuration to the OCT scan lens. To the best of our knowledge, this is the first time that UWF OCTA rat retinal images have been successfully acquired in a single shot. This novel scan lens optimizes the utilization of the inherent field aperture in rat retinal imaging, dramatically enlarging the FOV without compromis-

ing the image resolution compared to traditional 4f setups. The system's performance demonstrates its potential in rat retinal research, allowing for more comprehensive analysis of retinal vascular changes in both central and peripheral regions. The ability to conduct longitudinal studies offers a unique opportunity to observe time-dependent changes, disease progression, and potential retinal recovery that were previously difficult to capture.

Funding. National Institutes of Health (R01 EY036429, R01 EY024544, R01 EY027833, R01 EY031394, R01 EY035410, R01 HD107494, R01 EY010145, T32 EY023211, R43EY036781, P30 EY010572, UL1TR002369); The Jennie P. Weeks Endowed Fund; The Malcolm M. Marquis, MD Endowed Fund for Innovation; Unrestricted Departmental Funding Grant and Dr. H. James and Carole Free Catalyst Award from Research to Prevent Blindness (New York, NY); Edward N. and Della L. Thome Memorial Foundation Award; Bright Focus Foundation (G2020168, M20230081).

Disclosures. SN: Siloam Vision (P); YaJ: Optovue/Visionix, Inc. (P, R), Optos (P), Genentech, Inc. (P, R, F); JPC: Siloam Vision (P, F); YiJ: Siloam Vision (P, F). These potential conflicts of interest have been reviewed and managed by Oregon Health and Science University. Other authors declare no conflicts of interest related to this article.

Data availability. Data underlying the results presented in this paper are not publicly available at this time but may be obtained from the authors upon reasonable request.

Supplemental document. See *Supplement 1* for supporting content.

REFERENCES

1. M. Fruttiger, *Angiogenesis* **10**, 77 (2007).
2. A. Maass, P. L. von Leithner, V. Luong, *et al.*, *Curr. Eye Res.* **32**, 851 (2007).
3. Y. Geng, K. P. Greenberg, R. Wolfe, *et al.*, *Invest. Ophthalmol. Vis. Sci.* **50**, 5872 (2009).
4. J. D. Akula, T. L. Favazza, J. A. Mocko, *et al.*, *Doc. Ophthalmol.* **120**, 41 (2010).
5. R. Lee, T. Y. Wong, and C. Sabanayagam, *Eye Vis.* **2**, 17 (2015).
6. T. T. Hormel, G. B. Liang, X. Wei, *et al.*, *Opt. Express* **32**, 10329 (2024).
7. J. P. Kolb, T. Klein, C. L. Kufner, *et al.*, *Biomed. Opt. Express* **6**, 1534 (2015).
8. X. Wei, T. T. Hormel, Y. Guo, *et al.*, *Biomed. Opt. Express* **11**, 3234 (2020).
9. G. B. Liang, T. T. Hormel, X. Wei, *et al.*, *Biomed. Opt. Express* **14**, 5682 (2023).
10. S. Ni, X. Wei, R. Ng, *et al.*, *Biomed. Opt. Express* **12**, 3553 (2021).
11. X. Wei, T. T. Hormel, S. Pi, *et al.*, *Opt. Lett.* **47**, 5060 (2022).
12. J. Wang, A. Camino, X. Hua, *et al.*, *Biomed. Opt. Express* **10**, 120 (2019).
13. G. Kalra, F. Pichi, N. Kumar Menia, *et al.*, *Expert Rev. Med. Devices* **18**, 375 (2021).
14. S. Ni, T. P. Nguyen, R. Ng, *et al.*, *IEEE Trans. Med. Imaging* **42**, 3219 (2023).
15. D. Link, C. Strohmaier, B. U. Seifert, *et al.*, *Biomed. Opt. Express* **2**, 3094 (2011).
16. Y. Jian, K. Wong, and M. V. Sarunic, *J. Biomed. Opt.* **18**, 1 (2013).
17. Y. Jia, O. Tan, J. Tokayer, *et al.*, *Opt. Express* **20**, 4710 (2012).
18. Y. Guo, T. T. Hormel, S. Pi, *et al.*, *Biomed. Opt. Express* **12**, 4889 (2021).
19. C. B. Kim, P. A. D'Amore, and K. M. Connor, *Eye Brain* **8**, 67 (2016).
20. Y.-Q. Ni, X. Huang, K. Xue, *et al.*, *Invest. Ophthalmol. Vis. Sci.* **55**, 3165 (2014).
21. T.-H. Kim, T. Son, D. Le, *et al.*, *Sci. Rep.* **9**, 16685 (2019).